`

Isogenic hiPSC models of Turner syndrome development reveal shared roles of inactive X and Y in the human cranial neural crest network

Darcy T. Ahern [1,2] , Prakhar Bansal [1,2], Isaac V. Faustino [2], Heather R. Glatt-Deeley [2], Rachael Massey [1,2,3], Yuvabharath Kondaveeti [2], Erin C. Banda [2] and Stefan F. Pinter [1,2,3 *]

[1] Graduate Program in Genetics and Developmental Biology, UCONN Health, University of Connecticut, Farmington, CT, United States

[2] Department of Genetics and Genome Sciences, UCONN Health, University of Connecticut, Farmington, CT, United States

[3] Institute for Systems Genomics, University of Connecticut, Farmington, CT, United States

[*] Corresponding author: spinter@uchc.edu

`

SUMMARY

Modeling the developmental etiology of viable human aneuploidy can be challenging in rodents due to syntenic boundaries, or primate-specific biology. In humans, monosomy-X (45,X) causes Turner syndrome (TS), altering craniofacial, skeletal, endocrine, and cardiovascular development, which in contrast remain unaffected in 39,X-mice. To learn how human monosomy-X may impact early embryonic development, we turned to human 45,X and isogenic euploid induced pluripotent stem cells (hiPSCs) from male and female mosaic donors. Because neural crest (NC) derived cell types are hypothesized to underpin craniofacial and cardiovascular changes in TS, we performed a highly-powered differential expression study on hiPSC-derived anterior neural crest cells (NCCs). Across three independent isogenic panels, 45,X NCCs show impaired acquisition of $PAX7^{+}SOX10^{+}$ markers, and disrupted expression of other NCC-specific genes, relative to their isogenic euploid controls. In particular, 45,X NCCs increase cholesterol biosynthesis genes while reducing transcripts that feature 5' terminal oligopyrimidine (TOP) motifs, including those of ribosomal protein and nuclear-encoded mitochondrial genes. Such metabolic pathways are also over-represented in weighted co-expression gene modules that are preserved in monogenic neurocristopathy. Importantly, these gene modules are also significantly enriched in 28% of all TS-associated terms of the human phenotype ontology. Our analysis identifies specific sex-linked genes that are expressed from two copies in euploid males and females alike and qualify as candidate haploinsufficient drivers of TS phenotypes in NC-derived lineages. This study demonstrates that isogenic hiPSC-derived NCC panels representing monosomy-X can serve as a powerful model of early NC development in TS and inform new hypotheses towards its etiology.

`

59 **INTRODUCTION**

60 The absence of the second sex chromosome (monosomy-X) represents the only viable human
61 monosomy in humans, resulting in Turner syndrome (TS, 1:2000 live births). Although fewer than
62 0.3% of conceptuses with monosomy-X (45,X karyotype) complete development [1,2], it is
63 considered viable, because most sex-linked genes are expressed from a single copy in placental
64 mammals: the Y lost most of its ancestral genes originally shared with the proto-X, except for
65 dosage-sensitive regulators [3], while the X became subject to dosage-compensation in the form
66 of X chromosome inactivation (XCI) in XX females [4]. However, many genes retained on the Y have
67 a homologous X-linked copy that escapees XCI. In addition to these X/Y-pairs ("gametologs"),
68 genes in the recombining pseudoautosomal region (PAR) shared by X and Y also escape XCI in XX
69 females [4].

70 The compound haploinsufficiency of these gametolog and PAR genes is hypothesized to
71 underpin both cardinal short stature and premature ovarian failure in persons with TS, alongside
72 variably penetrant (40-80%) phenotypes [5], like lymphedema of hands and feet, neurocognitive
73 changes, as well as renal and cardiac malformations. Joining skeletal and craniofacial changes,
74 bicuspid aortic valve and aortic defects in TS implicate cell types derived from neural crest cells
75 (NCCs). These transitory multipotent progenitors arise from the dorsal side of the closing neural
76 tube and migrate ventrally to contribute to the developing face, skin, heart, adrenal glands, joints
77 and peripheral nervous system [6]. Because all of these organ systems are variably impacted in
78 subsets of TS patients [7], the neural crest is thought to be particularly vulnerable to monosomy-X.

79 Yet, direct experimental evidence for this hypothesis has been lacking. Because many murine
80 orthologs of human PAR genes reside on autosomes [8,9], their gene dosage is maintained in X-
81 monosomic mice, which consequently fail to model most TS phenotypes [10,11]. To address this
82 problem, we derived and cytogenomically validated X-monosomic human induced pluripotent
83 stem cells (hiPSCs) alongside isogenic euploid control lines from mosaic fibroblasts. We recently
84 reported that such isogenic panels from three unrelated donors recapitulate a hypothesized [2]
85 impairment of trophoblast cell fates due to monosomy-X [12].

86 Here, we derive anterior NCCs from each of these hiPSC panels to assess the impact of human
87 monosomy-X on the neural crest. We perform an in-depth transcriptomic and cellular analysis

`

88 comparing monosomy-X to their otherwise isogenic euploid controls, and find monosomy-X
89 hiPSCs give rise to significantly fewer PAX7/SOX10 double-positive NCCs compared to 46,XY
90 euploid controls. Differential expression reflecting monosomy-X is highly concordant across male
91 and female-derived panels, and jointly enriched in pathways associated with cholesterol
92 metabolism, NCC-relevant cell signaling, translation and mitochondrial function. Importantly,
93 NCC gene modules that reflect monosomy-X by weighted gene co-expression network analysis
94 (WGCNA) are also preserved in hiPSC-derived NCC models of monogenic conditions traditionally
95 considered to represent neurocristopathy.
96
97 **RESULTS**
98 Over half a century of detailed studies in the chick and other model systems have shed
99 light on the signaling pathways and intricate gene regulatory networks (GRNs) that govern the
100 specification and migration of NCCs [13,14]. These exquisite developmental studies have also
101 informed progressively intricate protocols for NCC derivation from embryonic stem cells and
102 hiPSCs that recapitulate terminal NCC fates as a function of their axial identity [15–17]. Due to our
103 interest in the anterior/craniofacial and vagal neural crest, which populate the developing face
104 and heart, we applied a highly robust method for NCC specification via moderate WNT and BMP
105 activation that is reported to enable reproducible derivation of anterior NCCs at ~ 70% efficiency
106 [17,18]. We applied this method to a total of 11 distinct hiPSC lines from all three of our
107 cytogenomically validated isogenic hiPSC panels [12], and quantified the dorsal neural tube marker
108 PAX7 alongside the canonical neural crest marker SOX10, which jointly mark NCC specification.
109 Applying automated immunofluorescence quantification, we observe the expected rate of $PAX7^+$
110 $SOX10^+$ double-positive cells (60-70%) across all euploid lines, though female euploid lines with
111 somewhat reduced efficiency relative to male euploid lines (Fig. 1A). While monosomy-X hiPSCs
112 can also differentiate to $PAX7^+SOX10^+$ NCCs, their overall efficiency is significantly reduced by
113 about half in both male-derived isogenic panels (Fig. 1B, male 1: $p=0.002$, male2: $p=1.1x10^{-5}$,
114 Mann-Whitney U). Interestingly, female-derived monosomy-X NCCs arise at a similar rate as their
115 euploid counterparts, rendering this isogenic comparison non-significant ($p=0.3$) but still
116 significantly reduced relative to male euploid controls ($p\leq1.3x10^{-3}$). Specifically, we find the $PAX7^+$

`

117 rate is largely unaffected by monosomy-X across all three panels (Fig. S1), whereas it is SOX10^{+} in
118 male1 and male2-derived monosomy-X lines that is significantly reduced (male 1: p=0.001,
119 male2: p=9.8 x10^{-6}, Mann-Whitney U).

120 We next performed a highly-powered RNA-seq study on a subset of these samples, with
121 a minimum of 4 replicates per cell line, grouped by a combination of donor and karyotype
122 ("condition"), comprising 7-12 replicates each. This enables our analysis to assess monosomy-X
123 driven changes within each isogenic context (or donor). Indeed, each paired set of 45,X and
124 euploid controls segregate from each other along the first and second principal components (Fig.
125 2A), while hierarchical clustering groups all male-derived monosomy-X samples together (Fig.
126 S2A). We next compared X-monosomic and euploid NCC expression levels of marker gene sets
127 identified in two prior human NCC differentiation studies [15,18], orthologs of chick neural crest
128 GRNs [19], and genes differentially expressed (DEGs) in the murine neural crest [20], as well DEGs of
129 a 3D *in vitro* model of the folding human neural tube [21]. Indeed, gene sets from these five studies
130 were largely sufficient to segregate euploid and X-monosomic samples (Fig. S2B). Single-cell DEGs
131 of the human 3D neural tube model were the most highly expressed, while early anterior neural
132 crest (eANC), murine Hox-negative NC markers, and migratory NC markers identified in the chick
133 were roughly tied. We also observed uniformly low expression of posterior HOX genes,
134 confirming the anterior identity of our NCCs (Fig. S2C). Assessing median-normalized gene set
135 levels, we observe significantly lower levels of early anterior neural crest (eANC) and higher levels
136 of late ANC (lANC) markers in euploid over X-monosomic lines in all three isogenic panels (Fig.
137 2B), and respectively higher expression of NC over neuroectodermal genes (NE) in male euploid
138 over X-monosomic NCCs (Fig. S2D). Likewise, genes expressed in p75^{+} hESC-derived NCCs are also
139 significantly higher in euploid over X-monosomic hiPSC-derived NCCs, which is also true for
140 orthologs of GRNs identified in the chick migratory neural crest (Fig. 2C,D).

141 To delineate which groups of X/Y-linked genes may be haploinsufficient in NCCs, we
142 plotted PAR and gametolog pair genes alongside X-specific genes that escaped XCI in female
143 euploid NCCs, as reflected in allelic variant counts of the phased female X (Fig. S2E). Largely driven
144 by PAR genes, monosomy-X NCCs segregate from their isogenic euploid controls, which
145 expectedly split female 46,XX and male 46,XY samples. DEGs escaping XCI in euploid female NCCs

`

146 (lesser allele frequency, LAF≥0.1, binomial p≤0.05) included 7 PAR1 genes, 5 X-linked gametologs
147 and 16 previously-reported escapee genes, alongside 8 genes that may reflect novel NCC-specific
148 escapees or have reactivated in a subset of cells despite robust bulk expression of *XIST* (Fig. S2F).
149 In male 46,XY hiPSCs, Y-linked gametologs generally trailed their X-linked homolog in expression
150 by a limited (~2-3) vst differential (Fig. S2G), with some nearly-equal (*NLGNX/Y & TXLNG/Y*) and
151 more divergent exceptions (*TMSB4X/Y, TBL1X/Y*). We next correlated the $PAX7^+$ $SOX10^+$ fraction
152 with the median expression of PAR, Pair, other escapee genes and their summed expression
153 ("All") in each sample (Fig. 2E). Including the NCC marker gene sets in this analysis, we observe
154 that the $PAX7^+$ $SOX10^+$ fraction best correlates with levels of PAR and Pair genes, which likewise
155 correlate with the late ANC, $p75^+$ and chick migratory GRN sets. Because NCC undergo an
156 epithelial-to-mesenchymal transition that modulates cell cycle progression [22,23], more mature
157 NCC markers are expectedly anti-correlated with cell cycle and earlier NCC markers. In sum, these
158 data suggest monosomy-X hinders or delays the maturation of early to late neural crest, in
159 keeping with their reduction of $SOX10^+$ positive cells.

160 To determine whether global differential expression points to a common monosomy-X
161 signature across isogenic panels, we called and compared DEGs common to any two or all three
162 panels. Altogether, over 30% of all DEGs were shared in all pairwise comparisons ($p = 1.1x10^{-13}$,
163 $p = 1.2x10^{-21}$ and $p = 3.7x10^{-137}$, hypergeometric test), with the two male-derived monosomy-X
164 panels reflecting the most significant overlap (Fig. 3A). We also assessed the direction of gene
165 expression changes in these overlapping DEG sets, which perfectly segregate all monosomy-X
166 samples from their isogenic euploid controls. Indeed, DEGs shared by all three ($p = 3.7x10^{-124}$,
167 sign test), as well as any two isogenic panels ($p = 7.4x10^{-195}$, $5.1x10^{-11}$, $8.0x10^{-47}$) change
168 concordantly in highly significant fashion (Fig. 3A). This level of overlap and concordant change
169 is remarkable given that monosomy-X samples ('mXO1/2' & 'fXO') were only assessed relative to
170 euploid controls in their own isogenic context.

171 To identify cellular pathways and developmental processes commonly impacted by the
172 lack of X or Y, we performed gene-set enrichment analysis (GSEA) for all three monosomy-X NCC
173 panels as ordered by their averaged Wald statistic ('ave.XO'). We also compared female-to-male
174 euploid ('fmE1/2'), as well karyotypically-identical male1-to-male2 monosomy-X ('m1m2O')

`

175 NCCs. Mirroring the global overlap of DEGs (Fig. 3A), significantly enriched gene-sets revealed a
176 highly concordant pattern across all three isogenic panels (Fig. 3B). Across Wikipathway
177 (p.adj<0.02), KEGG and Hallmark (Fig. S3, Table S1) gene term collections, monosomy-X NCCs
178 upregulate genes associated with cell cycle, cholesterol and lipid biosynthesis, and down-
179 regulate genes linked to translation and oxidative phosphorylation. While the impact of
180 monosomy-X in the female NCC panel is generally milder than the two male panels, the
181 concordance in GSEA terms mirrors the highly significant overlap in DEGs, and both
182 hyperlipidemia and hypercholesteremia are also seen in patients with TS [24]. Likewise, in the
183 human phenotype ontology (HPO), monosomy-X NCCs show dysregulated gene sets relating to
184 craniofacial, joint, and cognitive development that are also frequently observed in patients with
185 Turner Syndrome (Table S1), including 'Down-slated palpebral fissures', 'joint hypermobility,
186 'hyperactivity' (all p.adj<0.0001). Indeed, the enrichment of HPO terms relating to Turner
187 Syndrome ("ORPHA881") in monosomy-X NCC vs. control comparisons is particularly striking (Fig.
188 3C), and recovers 28/114 (24.6%) of all HPO terms linked to TS (Table S1), none of which were
189 significant in any of the control comparisons. In sum, these GSEA results underscore that
190 differential expression in X-monosomic NCCs relative to euploid controls recovers gene terms of
191 known TS phenotypes that relate to the neural crest, as well as beyond, and implicates cellular
192 and developmental pathways impacted by monosomy-X.

193 We next performed weighted gene co-expression network analysis (WGCNA) to elucidate
194 the relationships between monosomy-X and altered pathways, and prioritize individual X/Y-
195 linked genes as potential dosage-sensitive drivers. This analysis assigned genes to 29 modules,
196 23 of which are driven by contrasting expression of euploid and X-monosomic expression that
197 we define as a loss of module preservation (Z-score drop ≥5) in networks lacking euploid samples
198 (Fig. S4A). Eight modules (groupA: 1,6,7,13,19,20,26,27) are significantly correlated (R≥0.3,
199 p≤0.05) with the $PAX7^{+}SOX10^{+}$ rate, and six modules (groupB: 3,5,8,9,11,15) are significantly anti-
200 correlated (R≤–0.3, p≤0.05, Fig. 4A). Consistently, the $PAX7^{+}SOX10^{+}$ correlated groupA modules
201 associate with mature NCC markers, whereas $PAX7^{+}SOX10^{+}$ anti-correlated groupB modules
202 reflect an earlier, NE-biased cycling cell signature. The $PAX7^{+}SOX10^{+}$ positively-correlated groupA
203 was enriched in translation and mitochondrial function terms, while the $PAX7^{+}SOX10^{+}$ anti-

`

204 correlated groupB was over-represented for cholesterol biosynthesis, cell cycle-related terms,
205 and several signaling pathways, including p53, MAPK and mTOR signaling (Fig. 4A, S4B, Table S2).
206 To further contextualize the relationship between these modules and biological processes, we
207 turned to a semantic similarity map of significantly-enriched GO terms (p.adjust≤0.01,
208 hypergeometric distribution) in modules that also significantly co/anti-correlated with the
209 $PAX7^{+}SOX10^{+}$ rate (Fig. 4B, -/+ labeled modules). Terminal neural-crest related terms ("cranial
210 facial parasympathetic nerve", "endocardial cushion", "anterior/posterior pattern specification",
211 "angiogenesis") were enriched in groupB modules, whereas metabolic functions that connect cell
212 cycle and splicing to translation and mitochondrial function were represented by both group A&B
213 modules. Overall, these enriched metabolic terms mirrored the GSEA results (Fig. 3B, Table S1).
214 If the metabolic processes reflected in these modules play important roles in neural crest
215 development, we would expect them to be detectable in tissues populated by the neural crest.
216 We tested this hypothesis in transcriptomes collected from the developing heart [25] and face [26,27],
217 spanning Carnegie stages 13-23. Both tissues ('CS_Heart' with 11/28 preserved modules, and
218 'CS_Face' with 12/28) show moderate to high module preservation (Z-score ≥ 5), 8 of which also
219 co/anti-correlate significantly with the $PAX7^{+}SOX10^{+}$ rate in our hiPSC-derived NCCs (Fig. 4A).
220 Likewise, we assessed module preservation in hiPSC-derived NCCs of monogenic conditions
221 considered neurocristopathies: 15 modules were preserved in Waardenburg [28] (*SOX10*), 12 in
222 Pierre-Robin[29] (*SOX9*), and 11 each in Familial Dysautonomia[30] (*IKBKAP*) and Bohring-Opitz[31]
223 (*ASXL1*) syndromes, most of which also overlapped with each other. In contrast, only respectively
224 6 and 4 modules were preserved in hiPSC-derived NCC models of Floating-Harbor[32] (*SRCAP*) and
225 Branchio-Oculofacial[33] (*TFAP2A*) syndromes, while no module met the Z-score threshold in a
226 pancreatic tumor stroma control dataset. In sum, our analysis indicates that monosomy-X
227 sensitive modules that reflect metabolic disturbance also co-vary in relevant tissues with
228 developmental time and in NCC *in vitro* models of canonical neurocristopathies.
229 Interestingly, three groupA modules (13,20,27) were exclusively preserved in our hiPSC-
230 derived monosomy-X trophoblast model [12], and correlated with escapee levels (PAR, Pair &
231 'otherEsc'), as well as each other (Fig. 4A, S4C), raising the question in which modules these genes
232 were over-represented. Indeed, module 20 was strongly enriched in PAR genes (Fig. S4C) but

`

233 lacked any other significant MSigDB or GO annotations (Table S2). Likewise, most gametolog pairs
234 were dispersed across modules 4 & 20, or remained unassigned. One notable exception was the
235 only ribosomal protein to be encoded by two distinct genes, as *RPS4X* was assigned to the
236 translation-enriched module 6, which appeared generally down-regulated in X-monosomic lines
237 (Fig. 3B, Fig. 4A, Table S1).

238 To prioritize candidate dosage-sensitive genes shared by X and Y, we squared their
239 correlation with the averaged expression of their respective modules and plotted this coefficient
240 (kME^2) over their individual correlation with the $PAX7^{+}SOX10^{+}$ rate (Fig. 4C). We also present
241 their percentile-ranked probability of haploinsufficiency (pHI % rank, from[34]) as a constraint
242 metric to reflect possible selection. Most of the highly pHI-ranked genes correlate poorly with
243 the $PAX7^{+}SOX10^{+}$ percentage, in contrast to most PAR genes, as well as Y-linked gametologs, that
244 correlate strongly but rank expectedly low by pHI [35], by the residual variation intolerance score
245 (RVIS [36]), or remain unranked (Y-linked gametologs). Yet, *ZBED1, SLC25A6, RPS4X* and *PLCXD1,*
246 rank in the top half of pHI or RVIS scores and correlate strongly with the $PAX7^{+}SOX10^{+}$ rate and
247 their kME (Fig. 4C). While homozygous loss-of-function mutations have revealed *PLCXD1* as
248 dispensable in humans [37], *ZBED1* was also a top candidate in our 45,X hiPSC-derived trophoblast
249 analysis [12]. *RPS4X* was especially notable given that translation was over-represented in its
250 assigned module 6, which was also enriched in the three highest-scoring HPO terms associated
251 with TS: 'Horseshoe kidney', 'Coarctation of the aorta' and 'Webbed neck' (Fig. 4D). Altogether
252 32/114 (28.1%) of all TS-associated HPO terms were significantly enriched in 10 modules
253 (p.adjust≤0.1, hypergeometric distribution) (Fig. 4D, S4D), and 9 of these 10 modules were also
254 preserved in monogenic neurocristopathies (Fig. 4A).

255 Given the strong enrichment of ribosomal protein (RP) transcripts in module 6, and their
256 representation in the TS-associated HPO terms (Fig. 4D, Table S2), we sought to reconcile their
257 uniformly dampened expression with activation of mTOR signaling in 45,X NCCs (Fig. S4B). Active
258 mTOR boosts ribosome biogenesis by relieving the repressive impact of LARP1 on translation of
259 mRNAs with 5' UTR terminal oligopyrimidine (TOP) motifs [38]. However, LARP1 also stabilizes TOP-
260 motif transcripts via the small 40S ribosomal subunit, and depletion of either LARP1 or 40S
261 subunit RPs consequently destabilizes TOP-motif transcripts [39]. Because *RPS4X* is an essential

member of the 40S subunit, and is significantly reduced alongside *RPS4Y1* in male-derived 45,X NCCs (Fig. S2G), we asked whether TOP motif scores ("TOPscores", from [40]) were specifically predictive in our WGCNA or differential expression analysis. We find module 6 transcripts to feature significantly stronger TOPscores than the unassigned module, or indeed any of the other modules, even when removing RP genes (Fig. S4E, Mann-Whitney U $p = 2x10^{-56}$ and $p = 1.7x10^{-32}$ without RP genes). Many non-RP transcripts also contain TOP motifs, including those coding for mitochondrial proteins [41]. Indeed, several modules show a significant correlation between their transcripts' TOPscores and the $PAX7^{+}SOX10^{+}$ rate (Fig. 4E, S4E), including modules 1, 6, 19 and 25, which are also significantly enriched in nuclear-encoded mitochondrial proteins (Table S2). To determine whether TOP transcripts were specifically down-regulated in 45,X NCCs, we therefore compared the TOPscore of DEGs (down, up) to non-significant (ns) genes. Remarkably, median TOPscores across all WGCNA modules correlate significantly with the Wald statistic (Fig. 4F), and TOPscores of down-regulated transcripts are significantly higher (Mann-Whitney U $p=0.0235$, $p<2x10^{-16}$ for respective fXO and mXO1/2) than those of unchanged or up-regulated transcripts. In sum, these data support a specific depletion of TOP motif transcripts in 45,X NCCs, and are also consistent with an essential role of mTOR signaling in NCC specification, as recently reported [42].

DISCUSSION

Despite the relatively small number of genes shared by extant mammalian X & Y, to-date only TS-associated short stature has been linked conclusively to haploinsufficiency of one such gene, namely pseudoautosomal *SHOX* [43]. This example also highlights challenges in modeling TS in rodents, as murine *SHOX* ortholog *Shox2* is autosomal [44] and thus remains unaffected in 39,X mice, a pattern shared with all but two murine orthologs of human PAR1 genes [9]. Likewise, more pan-mammalian gametologs pairs were retained on both X&Y in humans than mice [3], with the remaining murine gametologs appearing largely haplo-sufficient in mouse cardiovascular development [10,11].

Given the craniofacial and cardiovascular phenotypes in TS, new models are thus needed to understand how monosomy-X impacts development, specifically in cells and tissues derived

`

291 from the neural crest. Our study applies a well-established hiPSC to NCC differentiation model
292 [17,18] to demonstrate that monosomy-X significantly reduces NCC specification relative to euploid
293 controls (Fig. 1, S1), which is also reflected in expression of various NC marker sets across three
294 independent isogenic panels (Fig. 2, S2). Differential expression indicates monosomy-X alters
295 important metabolic pathways, specifically increasing cholesterol biosynthesis genes, while
296 reducing RP and nuclear-encoded mitochondrial transcripts (Fig. 3, S3, Table S1). This finding is
297 consistent with recent reports revealing metabolic reprogramming to play a key role in
298 transitioning NCCs from proliferative to migratory and terminally differentiated states[45,46]. During
299 the epithelial-to-mesenchymal transition (EMT), NCCs increase both ribosome biosynthesis [45]
300 and aerobic glycolysis [46]. While glycolytic genes were upregulated in our 45,X NCC
301 transcriptomes, down-regulated transcripts included genes in oxidative phosphorylation, which
302 has also been linked to NCC specification [47] (Fig. 3, Table S1). In addition, cholesterol biosynthesis
303 genes are significantly upregulated in 45,X NCCs, which while critical for modulating NCC signaling
304 [48] may also alter their patterning [49], and is independently consistent with hypercholesteremia
305 seen in TS patients [5,24].

306 This link to TS phenotypes is also reflected in TS-associated HPO terms that were enriched
307 in GSEA (28/114) and WGCNA (32/114) results (Fig. 3,4). Indeed, three TS-associated HPO terms
308 were most significantly over-represented in module 6, which comprised transcripts for
309 mitochondrial and ribosomal proteins, as well as other cytosolic translation factors that appeared
310 to be reduced in 45,X NCCs. Because these transcripts feature strong TOP motifs, which are
311 bound and stabilized by LARP1 and the small 40S ribosomal subunit [39], we hypothesize that their
312 uniform reduction interferes with NCC specification. Indeed, the TOPscore was predictive of
313 specific modules' correlation with the $PAX7^{+}SOX10^{+}$ rate across samples (Fig. 4E), and the
314 likelihood that transcripts were down-regulated, rather than up-regulated or unchanged (Fig. 4F).
315 Together, these observations are consistent with the notion that the reduction in many TOP-
316 motif transcripts may block 45,X NCCs in a requisite step of metabolic reprogramming, despite
317 robust mTOR activation (Fig. S3, S4, Table S1).

318 Interestingly, RP gene and gametolog *RPS4X* was assigned to module 6, correlated with
319 the $PAX7^{+}SOX10^{+}$ rate, and ranks in the top half of pHI/RVIS scores among X-linked genes (Fig 4).

`

320 Although *RPS4X* is not implicated in cardinal TS phenotypes like short stature and gonadal
321 dysgenesis [50,51], we speculate that lower overall *RPS4X* and *RPS4Y1* dosage in 45,X NNCs may
322 reduce the production of 40S subunits, and thereby destabilize LARP1-bound TOP transcripts
323 required in NCC specification. In support of this notion, male-derived 45,X NCCs also reduced
324 *RPS4X* alongside other RP genes (Fig. S2G). One potential outcome of impaired ribosome
325 biogenesis is p53 activation, as in Diamond-Blackfan anemia due to haploinsufficient autosomal
326 RP genes, or craniofacial Treacher-Collins syndrome (*TCOF1*) due to defective rRNA production
327 [52]. Indeed, the p53 pathway is significantly upregulated in our male-derived 45,X NCCs (Fig. S3,
328 Table S1) and enriched in module 3 (Fig. S4B, Table S2). In contrast, female-derived 45,X NCCs
329 maintained a high degree of *RPS4X* expression from their single X, were less impacted overall
330 (Fig. 1), and did not upregulate the p53 pathway (Fig. S3), which may point to variation in *RPS4X*
331 levels as a potential source of previously noted variability of NC-related TS phenotypes [5].
332 To-date, escape of *RPS4X* from XCI has only been reported for primates [53], which have
333 also maintained *RPS4Y* on the Y [3]. Our study therefore raises the question whether neural-crest
334 related TS phenotypes may be more penetrant in mammals that also maintained Y-linked *RPS4Y*,
335 which may be resolved by comparative cardiovascular studies of mammals with sufficiently viable
336 monosomy-X that have a largely syntenic PAR but lack *RPS4Y* (e.g. horses) [9,54–56]. It is also
337 plausible that the neural crest may be sensitive to the dosage of multiple PAR genes and
338 gametologs, which poses challenges to prioritizing candidate dosage-sensitive genes by
339 mutational constraint measures that are based on the frequency of isolated loss-of-function
340 variants in the population. The GenTAC (Genetically Triggered Thoracic Aortic Aneurysms and
341 Other Cardiovascular Conditions) Registry reported that distal segmental Xp deletions minimally
342 encompassing PAR1 and 21 additional genes can be sufficient for bicuspid aortic valve and aortic
343 coarctation [57]. Interestingly, no such left-sided lesions were observed in 13 subjects non-mosaic
344 for 46,X,i(Xq) iso-chromosomes, pointing to increased Xq copy-number as a potential protective
345 factor when Xp dosage is lacking. Yet, as the iXq would be subject to XCI, such protective gene(s)
346 would also have to escape XCI. While this group of candidate protective genes is not necessarily
347 confined to gametologs, it should be noted that it only includes two such genes (*RPS4X, RBMX2)*
348 [58]. Looking forward, monosomy-X hiPSC-derived NCCs with otherwise isogenic euploid controls

`

349 provide a tractable model to resolve long-standing questions on the dosage contributions of
350 human PAR and gametolog pairs, and represent a platform to attribute clinically-relevant
351 features of TS to the dosage of specific genes in neural-crest derived cell types.

`

352 **FIGURE LEGENDS**
353
354 **Figure 1: Monosomy-X impact on neural crest differentiation relative to isogenic euploid**
355 **controls. (A)** Representative immunofluorescence (IF) of PAX7 (green), SOX10 (red) and nuclei
356 (Hoechst33342) in hiPSC-derived pairs of 45,X and euploid control NCCs from Male1/2 and
357 Female donors (100 um scale bar). **(B)** CellProfiler quantification of 4-7 rounds of differentiation.
358 Brackets and p-value (Mann-Whitney U test) indicate grouped cell lines compared within and
359 across isogenic panels (colored by donor, symbols denoting karyotype).
360
361 **Figure 2: Reduction of neural crest marker expression in monosomy-X relative isogenic euploid**
362 **controls. (A)** Principal component analysis (PCA) segregates samples by "condition" (donor &
363 karyotype), with % of variance of PC1/2 as indicated. **(B)** Variance-stabilized counts (vst) of early
364 and late anterior NC (e/lANC), retinoic acid-treated NC (raANC) and neuromesodermal progenitor
365 (NMP) markers from [18] (vertical panels) were median-normalized and averaged over euploid (EU)
366 and 45,X (XO) NCCs of each (horizontal) donor panel (significant differences denoted by Mann-
367 Whitney P-value). **(C,D)** as in B) for respectively p75-/+ associated markers [15], and chick NC
368 marker sets [19]. **(E)** Pearson correlation of the matching $PAX7^{+}SOX10^{+}$ percentage with averaged
369 marker sets from (B-D), alongside cycling markers [59], NC markers from a 3D folding human neural
370 tube model [21], and averaged pseudo-autosomal, X/Y Pair, and other escapee (PAR/PAIR/oESC)
371 expression. Only significant pairwise correlation shown ($p \leq 0.05$, Fisher transformed Pearson R).
372
373 **Figure 3: Concordant impact of monosomy-X on NCC transcriptomes across isogenic panels.**
374 **(A)** *Left:* Venn diagram of differentially expressed genes (DEGs) in male1, male2 and female
375 (mXO1, mXO2) 45,X NCCs. Significance of pairwise overlapping DEGs in bolded p-values
376 (hypergeometric distribution). *Right:* Differential vst heatmaps for overlapping DEG sets from (A)
377 as denoted by arrows. Ratio and p-value (sign-test) denote the number of DEGs with concordant
378 direction ("Dir.") in the triple and all pairwise overlapping DEG sets, also shown in divergent (fXO,
379 mXO1/2) annotation panels showing the Wald statistic (DESeq2) for each gene. Dendrogram
380 segregates samples by karyotype, irrespective of donor. **(B)** Wikipathway gene set enrichment
381 analysis (GSEA), ordered by the quantile-normalized mean Wald statistic across 45,X conditions
382 (ave.XO). X-axis denotes log-scaled GSEA adjusted p-value. Colored by normalized enrichment
383 score of up- (red) and down-(blue) regulated gene sets (sized by number of genes). Results for all
384 isogenic monosomy-X comparisons (fXO, mXO1/2), averaged (ave.XO/ave.mXO) and control
385 comparisons (fmE1/2: female-male euploids, and m1m2O: male1/2 45,X samples). **(C)** Human
386 Phenotype Ontology (HPO) GSEA results for significantly (p.adjust≤0.1) enriched terms associated
387 with Turner Syndrome (Orphanet ID: 881), ordered by the quantile-normalized mean (mXO1/2)
388 Wald statistic (ave.mXO, otherwise as in B).
389
390 **Figure 4: Monosomy-X sensitive gene modules correlate in human development and hiPSC-**
391 **derived NCC models of monogenic neurocristopathy. (A)** Color labels and genes per WGCNA
392 module (1-29) with corresponding: **(i)** Correlation matrix (Pearson R) of module eigengene to
393 karyotype status (euploid, 45,X) and $\%PAX7^{+}SOX10^{+}$, as well as averaged marker set expression,
394 and sex-linked genes (PAR, X/Y-pair, other escapees, and "All" classes combined). Only for
395 significant correlations ($p \leq 0.05$, Fisher transformation) shown, with log-scaled adjusted p-values

`

to the nearest integer. **(ii)** Significantly-enriched (p.adjust≤0.1, hypergeometric distribution) gene terms from the Hallmark and canonical pathways collections (MSigDB) representing metabolism and development. **(iii)** Preservation statistics (integer Z-score) in transcriptomes of the developing human face [26,27] (Carnegie stages CS13-17 & 22) and heart[25] (CS13-23), alongside hiPSC-derived NCC models of monogenic neurocristopathy syndromes (Pierre-Robin/*SOX9* [29], Waardenburg/*SOX10* [28], Familial Dysautonomia/*IKBKAP* [30], Bohring-Opitz/*ASXL1* [31], Floating-Harbor/*SRCAP* [32], and Branchio-Oculofacial/*TFAP2A* [33]). Monosomy-X human iPSC-derived trophoblast-like cells (TBL [12]) and pancreatic tumor stroma (Stroma [60]) as respective positive and negative controls. **(iv)** Module-averaged Wald statistic. **(B)** Enrichment map of significantly enriched gene ontology terms (GO, p.adjust≤0.01, hypergeometric distribution) as nodes. Genes shared between nodes (≥10%) depicted, based on semantic pairwise-term similarity (Jaccard distance) to cluster nodes and summarize labels. Nodes colored as pie charts by fraction of enriched modules under that term. **(C)** Module eigengene correlations (kME^2) for each sex-linked gene over its correlation with the $PAX7^{+}SOX10^{+}$ rate (colored by assigned module, sized by %pHI rank). **(D)** Dotplot of significantly-enriched (p.adjust ≤0.1, hypergeometric distribution) TS-HPO terms (x-axis, numeric module labels, above gene total). Dot color and size denote log-scaled adjusted p-value and fraction of term-associated genes per module. **(E)** Modules with significant correlation (R, with regression line and gray 95% C.I.) between genes' TOPscores (y-axis) and their Pearson coefficient with the $PAX7^{+}SOX10^{+}$ rate (x-axis), indicated by contour plots. **(F)** Median TOPscores over median Wald statistic by gene module (colors, size relative to gene total) with standard error bars per module. Pearson R correlation (black line, 95% C.I.) and p-value indicated for each comparison (fXO, mXO1 & mXO2), alongside TOPscores by DEG category (right).

`

SUPPLEMENTARY FIGURE LEGENDS

Figure S1: PAX7 and SOX10 quantification in isogenic monosomy-X and euploid control NCC differentiation panels. (A,B) Representative immunofluorescence (IF) images of hiPSC-derived pairs of monosomy-X alongside euploid control NCCs (from male2 and female donors) show PAX7 (green), SOX10 (red), nuclei (Hoechst33342) and merged channels (100 um scale bar). **(C,D)** CellProfiler IF quantification of all images from 4-7 rounds of differentiation across all cell lines. Brackets and p-value (Mann-Whitney U test) indicate groups of cell lines compared within each isogenic panel. Panels separate PAX7 and SOX10 percentages, as well as lines from each donor. Symbols and colors denote karyotype and donor.

Figure S2: RNA-seq samples, marker expression and allele-specific analysis for sex-linked genes. (A) Dendrogram of RNA-seq samples segregating by donor and karyotype. **(B)** NC-relevant marker gene sets clustered by median expression across each set. Plot facetted by donor, with karyotype indicated below dendrograms. **(C)** Expression levels (vst) of *HOXA* and *HOXB* cluster genes by condition. **(D)** Vst counts of NC and neuro-ectodermal (NE) markers, distinguished in a human 3D model of folding neural tube from [21], were median-normalized and averaged over euploid and 45,X (EU & XO, respectively) NC samples for each (horizontal) donor panel. Significant differences in median expression denoted by Mann-Whitney P-value. **(E)** Heatmap of median-normalized vst differential for PAR, X-pair, and other escapee genes, alongside their reported escapee status [58,61,62]. Left-most barplot annotation panels show each gene's allelic ratio in female euploid XX lines, and the three central barplot panels the log2FoldChange for differentially expressed gene (DESeq2 p.adjust≤0.1) in the three isogenic comparisons (fXO, mXO1, and mXO2, or 0 if not significant). **(F)** Expression levels (vst) of X-linked lncRNA genes *FIRRE, FTX, JPX* and *XIST* by condition. **(G)** as in (F) but for X/Y gametolog pairs.

Figure S3: (A) Gene set enrichment analysis (GSEA) results for the Hallmark collection, ordered the quantile-normalized mean Wald statistic across all monosomy-X conditions (ave.mXO). X axis denotes the log-scaled GSEA adjusted p-value, and colors the normalized enrichment score of up- (red) and down-(blue) regulated genes associated with a given term (bubble size depicts the corresponding number of genes). Results shown for all individual isogenic monosomy-X comparisons (fXO, mXO1/2), averaged (ave.XO/ave.mXO) Wald rankings and representative control comparisons (fmE1/2: female-to-male euploid, and m1m2O: male1/2 X-monosomic samples to each other). **(B)** GSEA results for the KEGG collection, otherwise as in A). **(C)** GSEA for the DESCARTES single-cell atlas, otherwise as in A).

`

Figure S4: WGCNA module preservation, eigengene correlation and term enrichments.
(A) Differential in Z-score preservation statistic after subtracting Z of a sample-size adjusted network (15 samples) across all karyotypes from corresponding Z of a network composed entirely of male-derived monosomy-X samples. Numeric labels and bar widths indicate module labels and size (gene total), respectively. **(B)** Dotplot of Hallmark and KEGG terms that were significantly-enriched (respectively, p.adjust≤0.05, hypergeometric distribution) in each module (x-axis, numeric module labels with gene totals in parentheses). Dot color and size denote log-scaled adjusted p-value and ratio of term-associated genes over all genes in each module. **(C)** Module eigengene correlations (kME, Pearson R) of sex-linked genes shared by X/Y or escaping XCI, alongside their reported escapee status (from [58,61,62]), and X-chromosomal region (PAR, non-PAR). Column annotations plot significantly enriched (log-scaled p-value, Fisher exact test) classes of sex-linked and/or XCI-escaping genes by module. **(D)** Enrichment map of significantly enriched HPO terms linked to TS (p.adjust≤0.1, hypergeometric distribution) as individually labeled nodes with edges drawn for shared genes (≥2%). Nodes are colored as pie charts by modules enriched for a given term, and the fraction of genes from each module under that term. **(E)** Cumulative distribution of genes' correlation coefficients with the $PAX7^{+}SOX10^{+}$ rate (top) by modules (colors), or genes' TOPscores (bottom). Mann-Whitney U test p-value (p) as indicated on plot for modules with significantly lower (9,28) and higher (6,13) TOPscore than the unassigned module (0). RP genes of modules 1 and 6 plotted separately (dashed lines).

Supplementary Tables:

Table S1: Gene-set enrichment analysis (GSEA) results for all monosomy X-relevant comparisons ("condition") across GO and selected MSigDB collections (Hallmark, canonical pathways, Human Phenotype Ontology & cell-type signatures). Lists normalized enrichment score (NES) and p.adjust for each comparison included for GSEA (ave.XO, ave.mXO, fXO, mXO1, mXO2, fmE1, fmE2 & m1m2O).

Table S2: Over-representation analysis (ORA) results for all WGCNA modules across selected GO and MSigDB collections (Hallmark, canonical pathways, Human Phenotype Ontology & cell-type signatures). Lists: ID, Description, GeneRatio, BgRatio and p.adjust for each module.

`

528 **MATERIALS AND METHODS**
529
530 **Human iPSC culture**
531 Euploid and X-monosomic hiPSC were derived from female and male donors, and
532 characterized for pluripotency markers, as well as DNA methylation and X-chromosome
533 inactivation in female euploid hiPSCs via continued *XIST* expression in RNA-seq as previously
534 described [12,63]. Human iPSCs were cultured in feeder-free conditions on GelTrex-coated plates
535 (ThermoFisher Scientific) in mTeSR-1 media (Stem Cell Technologies) in 5% CO_2 at 37°C. iPSCs
536 were passaged with 0.5M EDTA at least weekly in small aggregates.
537
538 **Neural Crest Cell Differentiation**
539 Confluent wells of iPSCs cultured on Geltrex-coated plates in mTeSR-1 medium were
540 singularized with Accutase (ThermoFisher Scientific) and plated on Geltrex coated plates at 4.5-
541 6 x10^4 cells/cm^2 in DMEM/F-12, 1x N2 (recipe modified from Waisman Center Intellectual &
542 Developmental Disabilities Research Center at University of Wisconsin-Madison: Insulin, 1.6
543 mg/mL; apo-Transferrin, 3.2 mg/mL; Putrescine, 0.5 mg/mL; Progesterone, 0.1 µg/mL; Sodium
544 selenite, 0.16 µg/mL (all from MilliporeSigma)), 1% Glutamax, 1% Non-essential Amino Acids, 1
545 µM CHIR99021 (StemCell Technologies), 2 µM SB431542 (StemCell Technologies), 1 µM DMH1
546 (Tocris Bioscience), 20 ng/mL BMP4 (Peprotech), and 10 µM Y-27632 (Tocris Bioscience), for the
547 first two days only. Media was changed daily until day 4 or 5 when the cells were harvested.
548
549 **Immunocytochemistry**
550 NCCs were fixed with 4% paraformaldehyde for 10 minutes at room temperature, washed
551 with 0.1% Triton-X, permeabilized with 1% Triton-X, blocked with 5% normal goat serum/2%
552 BSA/0.1% Triton-X for 1 hour and incubated with mouse monoclonal PAX7 antibody (abcam,
553 1:200) and rabbit monoclonal SOX10 antibody (Cell Signaling Technologies, 1:200) overnight at
554 4°C. The cells were then washed, incubated with AlexaFluor-555 Goat-anti-Mouse and AlexFluor-
555 647 Goat-anti-Rabbit Secondary Antibodies (Thermo Fisher Scientific, 1:500) for 1 hour at room
556 temperature. The cells were then washed, stained with Hoecsht-33342 diluted 1:10,000, and
557 mounted with ProLong Gold Antifade Mountant (ThermoFisher Scientific. The number of PAX7-
558 and SOX10-positive cells was imaged with an EVOS FL Auto system (ThermoFisher Scientific).
559
560 **Cell Profiler analysis**
561 The proportion of PAX7+ and SOX10+ cells was quantified by automated image analysis of
562 Hoechst-, PAX7-, and SOX10-stained slides using CellProfiler version 4.2.4 [64]. Nuclei were first
563 identified in the Hoechst channel, then the PAX7 and SOX10 channels were used to quantify the
564 number of PAX7+/SOX10+ double-positive, either single-positive type, and double-negative cells
565 per image. Illumination-corrected images were used for all channels, and nuclei outside the 10th
566 to 90th percentile size range for each Hoechst image were excluded. For each biological replicate,
567 the values from 3 fields of view were averaged to determine the percentage of single-positive,
568 and $PAX7^+SOX10^+$ double-positive cells, with an average of ~1000 nuclei counted for each
569 datapoint.
570
571

`

RNA-seq analysis

RNA was extracted from NCCs using the PureLink RNA Mini Kit (ThermoFisher Scientific). Libraries were prepared at the UConn Center for Genome Innovation using the Illumina Strand mRNA Kit and 100bp paired-ends reads were sequenced to an average depth of 40 million reads/replicate on the NovaSeq (Illumina).

Read pairs were trimmed using fastp [65], aligned to the human reference genome (hg38) using hisat2 [66] for allele-specific analysis of phased variants using phaser [67], and quantified against GENCODE version (v36) using salmon [68]. For analysis of XCI and escapee, A and B allele counts from phASER were tabulated and calls made by binomial test (lesser allele fraction, LAF > 0.1, $p \leq 0.05$) for all X-linked genes.

For differential expression using DESeq2 [69], salmon count tables were filtered for genes with sufficient expression. Surrogate variables were estimated using the sva package [70], and added to the DESeq2 design testing for condition and correcting for differentiation round. Gene-set enrichment analysis (GSEA) using clusterProfiler [71] was performed on all genes ranked by DESeq2's Wald statistic, as well as the average of the quantile-normalized Wald scores from the three euploid-45,X conditions (fXO, mXO1, mXO2) to ensure equal weighting.

Weighted gene co-expression network analysis (WGCNA) was performed on vst counts, using the WGCNA package [72], as a signed hybrid network using the biweight midcorrelation raised to a soft thresholding power of 12 (scale-free topology fit ≥ 0.85). Modules were correlated to $PAX7^{+}SOX10^{+}$ percentages and to averaged NCC lineage marker sets, which were median vst normalized to ensure equal weights across all sets. Module preservation analysis was performed against published RNA-seq datasets of the developing face [26,27], and heart [25], hiPSC-derived NCC models of Pierre-Robin [29], Waardenburg [28], Familial Dysautonomia [30], Bohring-Opitz [31], Floating-Harbor [32], and Branchio-Oculofacial [33] syndromes, as well as monosomy-X hiPSC-derived trophoblast-like cells [12] and pancreatic tumor stroma [60]. Overrepresentation analysis of gene terms across WGCNA modules was performed with clusterProfiler [71].

ACKNOWLEDGMENTS

We would like to thank the Cotney lab at UConn Health for early access to transcriptome data from the developing face, and Bo Reese at the UConn Center for Genome Innovation for mRNA-seq library preparation and sequencing. This work was supported by NIH grants R35GM124926 and R01HL141324 to S.F.P.

`

616 **REFERENCES**

617 1. Hook, E. B. & Warburton, D. The distribution of chromosomal genotypes associated with
618 Turner's syndrome: livebirth prevalence rates and evidence for diminished fetal mortality
619 and severity in genotypes associated with structural X abnormalities or mosaicism. *Hum.*
620 *Genet.* **64**, 24–7 (1983).

621 2. Hook, E. B. & Warburton, D. Turner syndrome revisited: review of new data supports the
622 hypothesis that all viable 45,X cases are cryptic mosaics with a rescue cell line, implying
623 an origin by mitotic loss. *Hum. Genet.* **133**, 417–24 (2014).

624 3. Bellott, D. W., Hughes, J. F., Skaletsky, H., Brown, L. G., Pyntikova, T., Cho, T.-J., *et al.*
625 Mammalian Y chromosomes retain widely expressed dosage-sensitive regulators. *Nature*
626 **508**, 494–9 (2014).

627 4. Posynick, B. J. & Brown, C. J. Escape From X-Chromosome Inactivation: An Evolutionary
628 Perspective. *Front. Cell Dev. Biol.* **7**, 241 (2019).

629 5. Gravholt, C. H., Viuff, M. H., Brun, S., Stochholm, K. & Andersen, N. H. Turner syndrome:
630 mechanisms and management. *Nat. Rev. Endocrinol.* **15**, 601–614 (2019).

631 6. Tang, W. & Bronner, M. E. Neural crest lineage analysis: From past to future trajectory.
632 *Dev.* **147**, (2021).

633 7. Gravholt, C. H., Viuff, M., Just, J., Sandahl, K., Brun, S., van der Velden, J., *et al.* The
634 Changing Face of Turner Syndrome. *Endocr. Rev.* **44**, 33–69 (2023).

635 8. Perry, J., Palmer, S., Gabriel, A. & Ashworth, A. A short pseudoautosomal region in
636 laboratory mice. *Genome Res.* **11**, 1826–32 (2001).

637 9. Raudsepp, T. & Chowdhary, B. P. The Eutherian Pseudoautosomal Region. *Cytogenet.*
638 *Genome Res.* (2016) doi:10.1159/000443157.

639 10. Lynn, P. M. Y. & Davies, W. The 39,XO mouse as a model for the neurobiology of Turner
640 syndrome and sex-biased neuropsychiatric disorders. *Behavioural Brain Research* vol.
641 179 173–182 (2007).

642 11. Probst, F. J., Cooper, M. L., Cheung, S. W. & Justice, M. J. Genotype, phenotype, and
643 karyotype correlation in the XO mouse model of turner syndrome. *J. Hered.* **99**, 512–517
644 (2008).

645 12. Ahern, D. T., Bansal, P., Armillei, M. K., Faustino, I. V., Kondaveeti, Y., Glatt-Deeley, H. R.,
646 *et al.* Monosomy X in isogenic human iPSC-derived trophoblast model impacts expression
647 modules preserved in human placenta. *Proc. Natl. Acad. Sci.* **119**, e2211073119 (2022).

648 13. Rothstein, M., Bhattacharya, D. & Simoes-Costa, M. The molecular basis of neural crest
649 axial identity. *Dev. Biol.* **444**, S170–S180 (2018).

650 14. Etchevers, H. C., Dupin, E. & Le Douarin, N. M. The diverse neural crest: From embryology
651 to human pathology. *Dev.* **146**, (2019).

652 15. Lee, G., Kim, H., Elkabetz, Y., Al Shamy, G., Panagiotakos, G., Barberi, T., *et al.* Isolation
653 and directed differentiation of neural crest stem cells derived from human embryonic

654 stem cells. *Nat. Biotechnol.* **25**, 1468–1475 (2007).

655 16. Leung, A. W., Leung, A. W., Murdoch, B., Salem, A. F., Prasad, M. S., Gomez, G. A., *et al.*
656 WNT/β-catenin signaling mediates human neural crest induction via a pre-neural border
657 intermediate. *Dev.* **143**, 398–410 (2016).

658 17. Hackland, J. O. S., Frith, T. J. R., Thompson, O., Marin Navarro, A., Garcia-Castro, M. I.,
659 Unger, C., *et al.* Top-Down Inhibition of BMP Signaling Enables Robust Induction of hPSCs
660 Into Neural Crest in Fully Defined, Xeno-free Conditions. *Stem Cell Reports* **9**, 1043–1052
661 (2017).

662 18. Frith, T. J., Granata, I., Wind, M., Stout, E., Thompson, O., Neumann, K., *et al.* Human
663 axial progenitors generate trunk neural crest cells in vitro. *Elife* **7**, (2018).

664 19. Simões-Costa, M. & Bronner, M. E. Establishing neural crest identity: a gene regulatory
665 recipe. *Development* **142**, 242–257 (2015).

666 20. Soldatov, R., Kaucka, M., Kastriti, M. E., Petersen, J., Chontorotzea, T., Englmaier, L., *et al.*
667 Spatiotemporal structure of cell fate decisions in murine neural crest. *Science (80-.).* **364**,
668 (2019).

669 21. Karzbrun, E., Khankhel, A. H., Megale, H. C., Glasauer, S. M. K., Wyle, Y., Britton, G., *et al.*
670 Human neural tube morphogenesis in vitro by geometric constraints. *Nat. 2021 5997884*
671 **599**, 268–272 (2021).

672 22. Vega, S., Morales, A. V., Ocaña, O. H., Valdés, F., Fabregat, I. & Nieto, M. A. Snail blocks
673 the cell cycle and confers resistance to cell death. *Genes Dev.* **18**, 1131–1143 (2004).

674 23. Thiery, J. P., Acloque, H., Huang, R. Y. J. & Nieto, M. A. Epithelial-Mesenchymal
675 Transitions in Development and Disease. *Cell* **139**, 871–890 (2009).

676 24. Lebenthal, Y., Levy, S., Sofrin-Drucker, E., Nagelberg, N., Weintrob, N., Shalitin, S., *et al.*
677 The Natural History of Metabolic Comorbidities in Turner Syndrome from Childhood to
678 Early Adulthood: Comparison between 45,X Monosomy and Other Karyotypes. *Front.*
679 *Endocrinol. (Lausanne).* **9**, 27 (2018).

680 25. Vanoudenhove, J., Yankee, T. N., Wilderman, A. & Cotney, J. Epigenomic and
681 Transcriptomic Dynamics During Human Heart Organogenesis. *Circ. Res.* **127**, E184–E209
682 (2020).

683 26. Yankee, T. N., Oh, S., Winchester, E. W., Wilderman, A., Robinson, K., Gordon, T., *et al.*
684 Integrative analysis of transcriptome dynamics during human craniofacial development
685 identifies candidate disease genes. *Nat. Commun. 2023 141* **14**, 1–23 (2023).

686 27. Brinkley, J. F., Fisher, S., Harris, M. P., Holmes, G., Hooper, J. E., Jabs, E. W., *et al.* The
687 facebase consortium: A comprehensive resource for craniofacial researchers. *Dev.* **143**,
688 2677–2688 (2016).

689 28. Wen, J., Song, J., Bai, Y., Liu, Y., Cai, X., Mei, L., *et al.* A Model of Waardenburg Syndrome
690 Using Patient-Derived iPSCs With a SOX10 Mutation Displays Compromised Maturation
691 and Function of the Neural Crest That Involves Inner Ear Development. *Front. cell Dev.*

Biol. **9**, (2021).

29. Long, H. K., Osterwalder, M., Welsh, I. C., Hansen, K., Davies, J. O. J., Liu, Y. E., *et al.* Loss of Extreme Long-Range Enhancers in Human Neural Crest Drives a Craniofacial Disorder. *Cell Stem Cell* **27**, 765-783.e14 (2020).

30. Zeltner, N., Fattahi, F., Dubois, N. C., Saurat, N., Lafaille, F., Shang, L., *et al.* Capturing the biology of disease severity in a PSC-based model of familial dysautonomia. *Nat. Med.* **22**, 1421–1427 (2016).

31. Matheus, F., Rusha, E., Rehimi, R., Molitor, L., Pertek, A., Modic, M., *et al.* Pathological ASXL1 Mutations and Protein Variants Impair Neural Crest Development. *Stem cell reports* **12**, 861–868 (2019).

32. Greenberg, R. S., Long, H. K., Swigut, T. & Wysocka, J. Single Amino Acid Change Underlies Distinct Roles of H2A.Z Subtypes in Human Syndrome. *Cell* **178**, 1421-1436.e24 (2019).

33. Laugsch, M., Bartusel, M., Rehimi, R., Alirzayeva, H., Karaolidou, A., Crispatzu, G., *et al.* Modeling the Pathological Long-Range Regulatory Effects of Human Structural Variation with Patient-Specific hiPSCs. *Cell Stem Cell* **24**, 736-752.e12 (2019).

34. Roman, A. K. S., Godfrey, A. K., Skaletsky, H., Bellott, D. W., Groff, A. F., Harris, H. L., *et al.* The human inactive X chromosome modulates expression of the active X chromosome. *Cell Genomics* **3**, 100259 (2023).

35. Huang, N., Lee, I., Marcotte, E. M. & Hurles, M. E. Characterising and Predicting Haploinsufficiency in the Human Genome. *PLOS Genet.* **6**, e1001154 (2010).

36. Petrovski, S., Wang, Q., Heinzen, E. L., Allen, A. S. & Goldstein, D. B. Genic Intolerance to Functional Variation and the Interpretation of Personal Genomes. *PLOS Genet.* **9**, e1003709 (2013).

37. Karczewski, K. J., Francioli, L. C., Tiao, G., Cummings, B. B., Alföldi, J., Wang, Q., *et al.* The mutational constraint spectrum quantified from variation in 141,456 humans. *Nat. 2020 5817809* **581**, 434–443 (2020).

38. Hong, S., Freeberg, M. A., Han, T., Kamath, A., Yao, Y., Fukuda, T., *et al.* LARP1 functions as a molecular switch for mTORC1-mediated translation of an essential class of mRNAs. *Elife* **6**, (2017).

39. Gentilella, A., Morón-Duran, F. D., Fuentes, P., Rocha, G. Z., Riaño-Canalias, F., Pelletier, J., *et al.* Autogenous Control of 5'TOP mRNA Stability by 40S Ribosomes. *Mol. Cell* **67**, 55-70.e4 (2017).

40. Philippe, L., van den Elzen, A. M. G., Watson, M. J. & Thoreen, C. C. Global analysis of LARP1 translation targets reveals tunable and dynamic features of 5' TOP motifs. *Proc. Natl. Acad. Sci. U. S. A.* **117**, 5319–5328 (2020).

41. Gandin, V., Masvidal, L., Hulea, L., Gravel, S. P., Cargnello, M., McLaughlan, S., *et al.* NanoCAGE reveals 5' UTR features that define specific modes of translation of

730 functionally related MTOR-sensitive mRNAs. *Genome Res.* **26**, 636–648 (2016).

731 42. Nie, X., Ricupero, C. L., Jiao, K., Yang, P. & Mao, J. J. mTOR deletion in neural crest cells
732 disrupts cardiac outflow tract remodeling and causes a spectrum of cardiac defects
733 through the mTORC1 pathway. *Dev. Biol.* **477**, 241–250 (2021).

734 43. Rao, E., Weiss, B., Fukami, M., Rump, A., Niesler, B., Mertz, A., *et al.* Pseudoautosomal
735 deletions encompassing a novel homeobox gene cause growth failure in idiopathic short
736 stature and Turner syndrome. *Nat. Genet.* **16**, 54–63 (1997).

737 44. Cobb, J., Dierich, A., Huss-Garcia, Y. & Duboule, D. A mouse model for human short-
738 stature syndromes identifies Shox2 as an upstream regulator of Runx2 during long-bone
739 development. *Proc. Natl. Acad. Sci. U. S. A.* **103**, 4511–5 (2006).

740 45. Prakash, V., Carson, B. B., Feenstra, J. M., Dass, R. A., Sekyrova, P., Hoshino, A., *et al.*
741 Ribosome biogenesis during cell cycle arrest fuels EMT in development and disease. *Nat.*
742 *Commun. 2019 101* **10**, 1–16 (2019).

743 46. Bhattacharya, D., Azambuja, A. P. & Simoes-Costa, M. Metabolic Reprogramming
744 Promotes Neural Crest Migration via Yap/Tead Signaling. *Dev. Cell* **53**, 199-211.e6 (2020).

745 47. Costa, R., Muccioli, S., Brillo, V., Bachmann, M., Szabò, I. & Leanza, L. Mitochondrial
746 dysfunction interferes with neural crest specification through the FoxD3 transcription
747 factor. *Pharmacol. Res.* **164**, (2021).

748 48. Castro, V. L., Reyes-Nava, N. G., Sanchez, B. B., Gonzalez, C. G., Paz, D. & Quintana, A. M.
749 Activation of WNT signaling restores the facial deficits in a zebrafish with defects in
750 cholesterol metabolism. *genesis* **58**, e23397 (2020).

751 49. Bhattacharya, D., Khan, B. & Simoes-Costa, M. Neural crest metabolism: At the
752 crossroads of development and disease. *Dev. Biol.* **475**, 245–255 (2021).

753 50. Omoe, K. & Endo, A. Relationship between the monosomy X phenotype and Y-linked
754 ribosomal protein S4 (Rps4) in several species of mammals: a molecular evolutionary
755 analysis of Rps4 homologs. *Genomics* **31**, 44–50 (1996).

756 51. Geerkens, C., Just, W., Held, K. R. & Vogel, W. Ullrich-Turner syndrome is not caused by
757 haploinsufficiency of RPS4X. *Hum. Genet. 1996 971* **97**, 39–44 (1996).

758 52. Da Costa, L., Mohandas, N., David-NGuyen, L., Platon, J., Marie, I., O'Donohue, M. F., *et*
759 *al.* Diamond-Blackfan anemia, the archetype of ribosomopathy: How distinct is it from
760 the other constitutional ribosomopathies? *Blood Cells, Mol. Dis.* **106**, 102838 (2024).

761 53. Balaton, B. P., Fornes, O., Wasserman, W. W. & Brown, C. J. Cross-species examination of
762 X-chromosome inactivation highlights domains of escape from silencing. *Epigenetics and*
763 *Chromatin* **14**, 12 (2021).

764 54. Bugno-Poniewierska, M. & Raudsepp, T. Horse Clinical Cytogenetics: Recurrent Themes
765 and Novel Findings. *Anim. an Open Access J. from MDPI* **11**, 1–26 (2021).

766 55. Szczerbal, I. & Switonski, M. Genetic disorders of sex development in cats: An update.
767 *Anim. Reprod. Sci.* **216**, 106353 (2020).

`

768 56. Li, G., Davis, B. W., Raudsepp, T., Pearks Wilkerson, A. J., Mason, V. C., Ferguson-Smith,
769 M., *et al.* Comparative analysis of mammalian Y chromosomes illuminates ancestral
770 structure and lineage-specific evolution. *Genome Res.* **23**, 1486–95 (2013).

771 57. Prakash, S. K., Bondy, C. A., Maslen, C. L., Silberbach, M., Lin, A. E., Perrone, L., *et al.*
772 Autosomal and X chromosome structural variants are associated with congenital heart
773 defects in Turner syndrome: The NHLBI GenTAC registry. *Am. J. Med. Genet. Part A* **170**,
774 3157–3164 (2016).

775 58. Tukiainen, T., Villani, A.-C., Yen, A., Rivas, M. A., Marshall, J. L., Satija, R., *et al.* Landscape
776 of X chromosome inactivation across human tissues. *Nature* **550**, 244–248 (2017).

777 59. Hsiao, C. J., Tung, P. Y., Blischak, J. D., Burnett, J. E., Barr, K. A., Dey, K. K., *et al.*
778 Characterizing and inferring quantitative cell cycle phase in single-cell RNA-seq data
779 analysis. *Genome Res.* **30**, 611–621 (2020).

780 60. Birnbaum, D. J., Begg, S. K. S., Finetti, P., Vanderburg, C., Kulkarni, A. S., Neyaz, A., *et al.*
781 Transcriptomic Analysis of Laser Capture Microdissected Tumors Reveals Cancer- and
782 Stromal-Specific Molecular Subtypes of Pancreatic Ductal Adenocarcinoma. *Clin. Cancer*
783 *Res.* **27**, 2314–2325 (2021).

784 61. Wainer Katsir, K. & Linial, M. Human genes escaping X-inactivation revealed by single cell
785 expression data. *BMC Genomics* **20**, 1–17 (2019).

786 62. Sauteraud, R., Stahl, J. M., James, J., Englebright, M., Chen, F., Zhan, X., *et al.* Inferring
787 genes that escape X-Chromosome inactivation reveals important contribution of variable
788 escape genes to sex-biased diseases. *Genome Res.* **31**, 1629–1637 (2021).

789 63. Bansal, P., Ahern, D. T., Kondaveeti, Y., Qiu, C. W. & Pinter, S. F. Contiguous erosion of
790 the inactive X in human pluripotency concludes with global DNA hypomethylation. *Cell*
791 *Rep.* **35**, 109215 (2021).

792 64. Mcquin, C., Goodman, A., Chernyshev, V., Kamentsky, L., Cimini, A., Karhohs, K. W., *et al.*
793 Cellprofiler 3.0. *PLoS Biol.* 1–17 (2018).

794 65. Chen, S., Zhou, Y., Chen, Y. & Gu, J. fastp: an ultra-fast all-in-one FASTQ preprocessor.
795 *Bioinformatics* **34**, i884–i890 (2018).

796 66. Kim, D., Paggi, J. M., Park, C., Bennett, C. & Salzberg, S. L. Graph-based genome
797 alignment and genotyping with HISAT2 and HISAT-genotype. *Nat. Biotechnol.* **37**, 907–
798 915 (2019).

799 67. Castel, S. E., Mohammadi, P., Chung, W. K., Shen, Y. & Lappalainen, T. Rare variant
800 phasing and haplotypic expression from RNA sequencing with phASER. *Nat. Commun.* **7**,
801 1–6 (2016).

802 68. Patro, R., Duggal, G., Love, M. I., Irizarry, R. A. & Kingsford, C. Salmon provides fast and
803 bias-aware quantification of transcript expression. *Nat. Methods* **14**, 417–419 (2017).

804 69. Love, M. I., Huber, W. & Anders, S. Moderated estimation of fold change and dispersion
805 for RNA-seq data with DESeq2. *Genome Biol.* **15**, (2014).

`

806 70. Leek, J. T., Johnson, W. E., Parker, H. S., Jaffe, A. E. & Storey, J. D. The SVA package for
807 removing batch effects and other unwanted variation in high-throughput experiments.
808 *Bioinformatics* **28**, 882–883 (2012).

809 71. Yu, G., Wang, L.-G., Han, Y. & He, Q.-Y. clusterProfiler: an R Package for Comparing
810 Biological Themes Among Gene Clusters. *OMICS: A Journal of Integrative Biology* vol. 16
811 284–287 (2012).

812 72. Langfelder, P. & Horvath, S. WGCNA: An R package for weighted correlation network
813 analysis. *BMC Bioinformatics* **9**, 1–13 (2008).

814

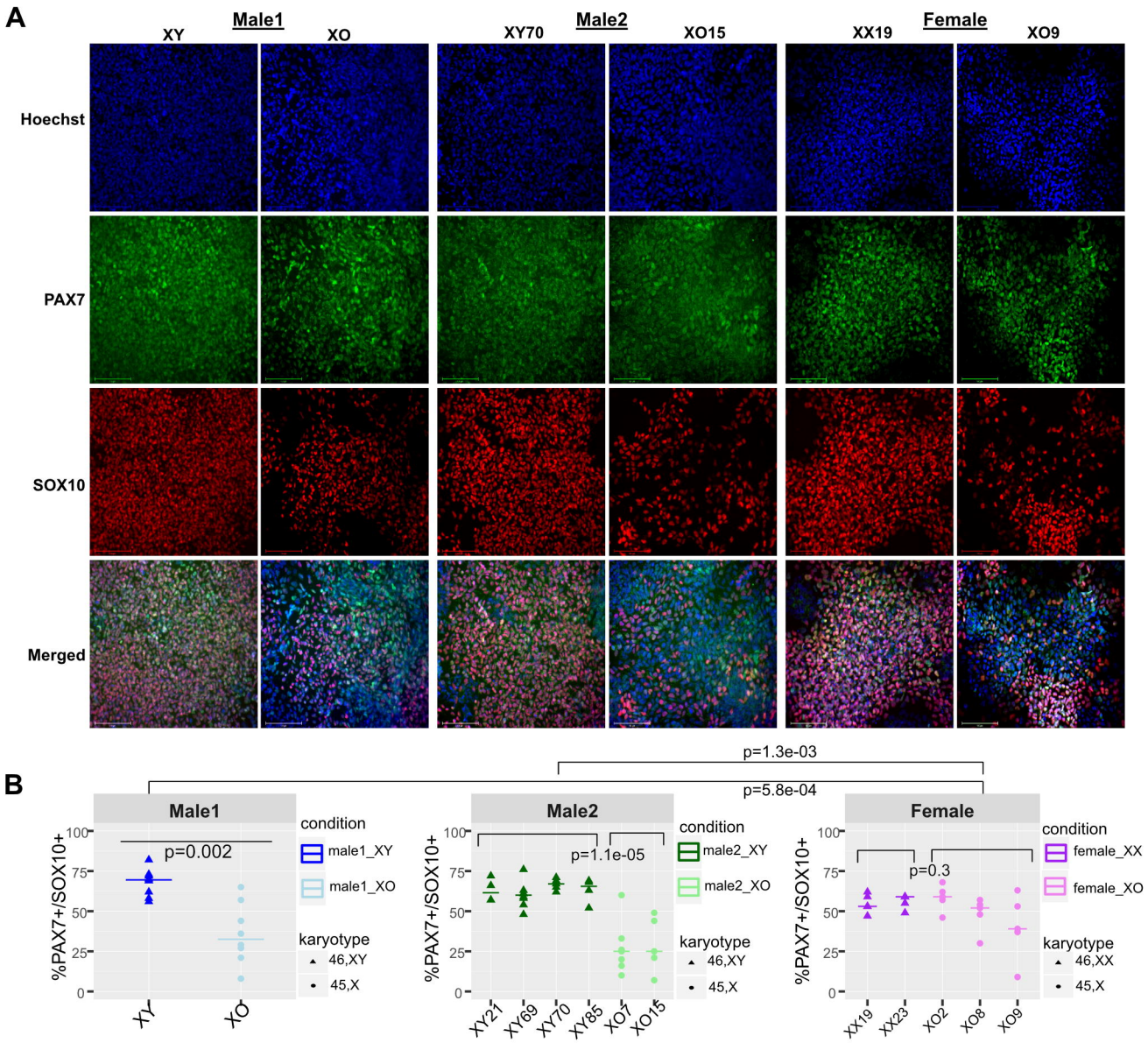
A
Male1
XY
XO
Male2
XY70
XO15
Female
XX19
XO9
Hoechst
PAX7
SOX10
Merged
B
p=1.3e-03
p=5.8e-04
Male1
p=0.002
%PAX7+/SOX10+
condition
male1_XY
male1_XO
karyotype
46,XY
45,X
XY
XO
Male2
p=1.1e-05
male2_XY
male2_XO
XY21
XY69
XY70
XY85
XO7
XO15
Female
p=0.3
female_XX
female_XO
46,XX
XX19
XX23
XO2
XO8
XO9

Figure 1

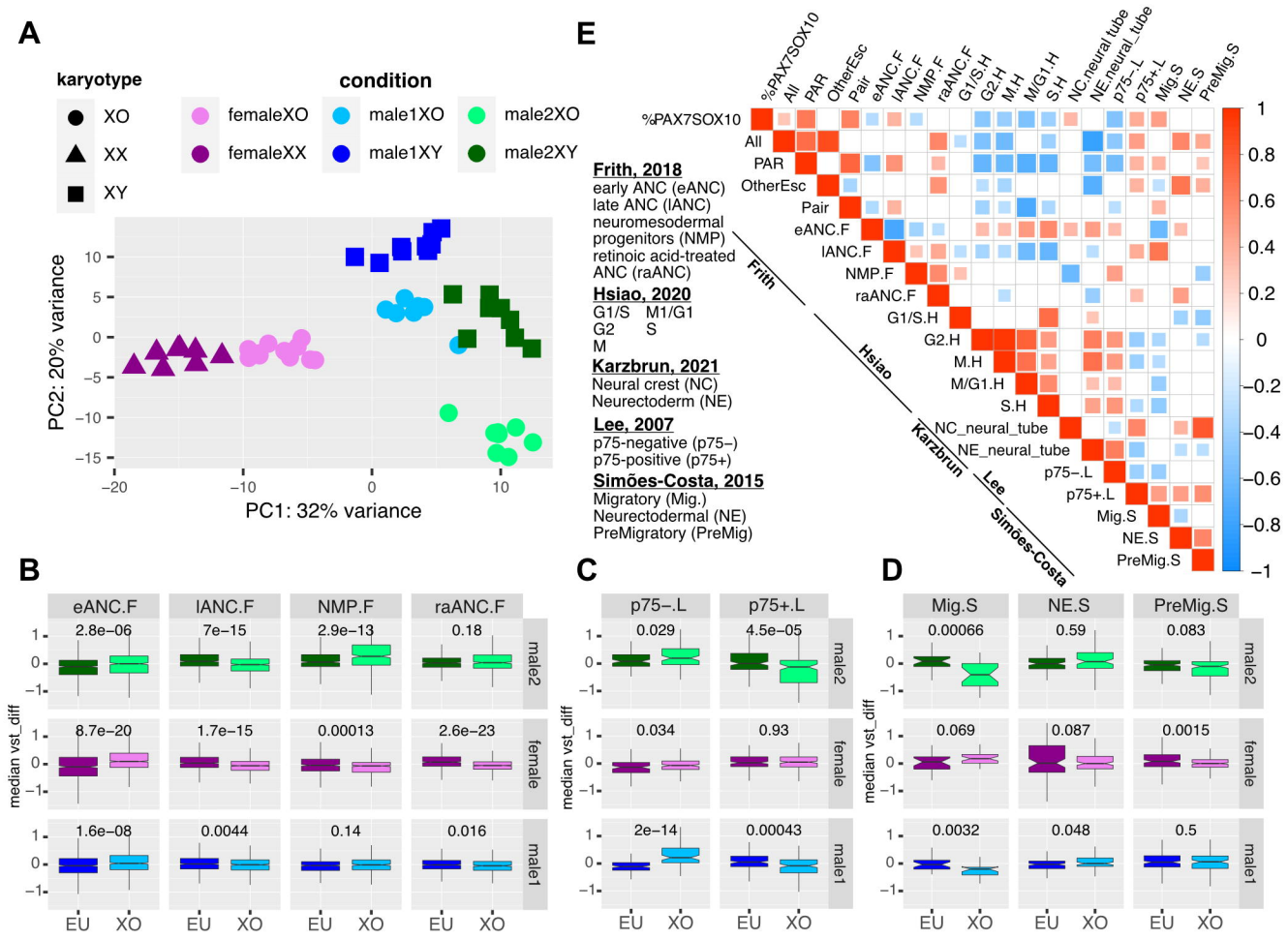
A
karyotype
XO
XX
XY
condition
femaleXO
femaleXX
male1XO
male1XY
male2XO
male2XY
PC2: 20% variance
PC1: 32% variance
E
%PAX7SOX10
All
PAR
OtherEsc
Pair
eANC.F
lANC.F
NMP.F
raANC.F
G1/S.H
G2.H
M.H
M/G1.H
S.H
NC.neural tube
NE.neural_tube
p75−.L
p75+.L
Mig.S
NE.S
PreMig.S
Frith, 2018
early ANC (eANC)
late ANC (lANC)
neuromesodermal progenitors (NMP)
retinoic acid-treated ANC (raANC)
Hsiao, 2020
G1/S M1/G1
G2 S
M
Karzbrun, 2021
Neural crest (NC)
Neurectoderm (NE)
Lee, 2007
p75-negative (p75−)
p75-positive (p75+)
Simões-Costa, 2015
Migratory (Mig.)
Neurectodermal (NE)
PreMigratory (PreMig)
Frith
Hsiao
Karzbrun
Lee
Simões-Costa
B
C
D
median vst_diff
male2
female
male1
EU
XO

Figure 2

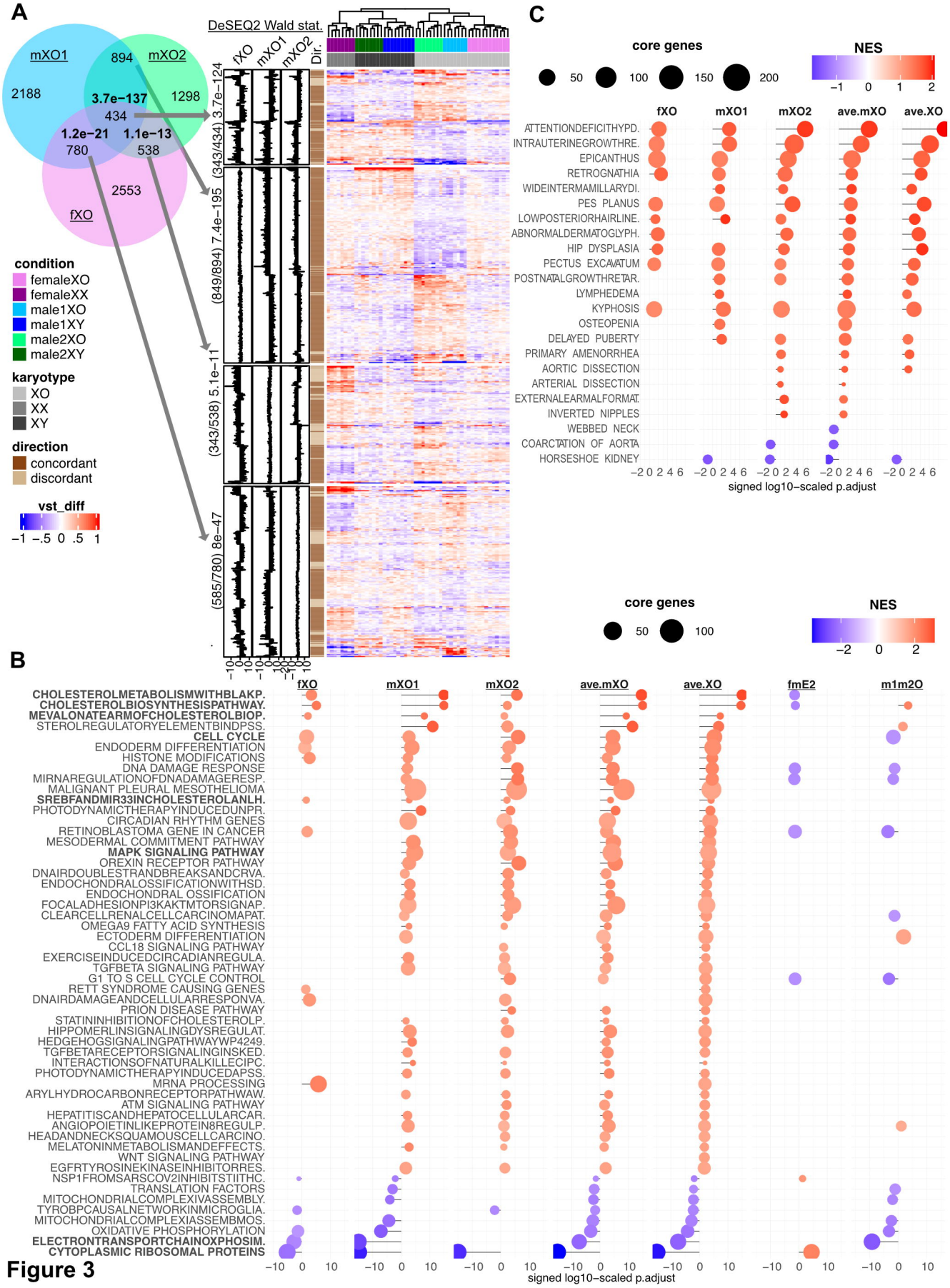
A
mXO1
mXO2
fXO
2188
894
1298
3.7e−137
434
1.2e−21
780
1.1e−13
538
2553
condition
femaleXO
femaleXX
male1XO
male1XY
male2XO
male2XY
karyotype
XO
XX
XY
direction
concordant
discordant
vst_diff
−1 −.5 0 .5 1
DeSEQ2 Wald stat.
fXO
mXO1
mXO2
Dir.
(343/434) 3.7e−124
(849/894) 7.4e−195
(343/538) 5.1e−11
(585/780) 8e−47
C
core genes
50
100
150
200
NES
−1 0 1 2
fXO
mXO1
mXO2
ave.mXO
ave.XO
ATTENTIONDEFICITHYPD.
INTRAUTERINEGROWTHRE.
EPICANTHUS
RETROGNATHIA
WIDEINTERMAMILLARYDI.
PES PLANUS
LOWPOSTERIORHAIRLINE.
ABNORMALDERMATOGLYPH.
HIP DYSPLASIA
PECTUS EXCAVATUM
POSTNATALGROWTHRETAR.
LYMPHEDEMA
KYPHOSIS
OSTEOPENIA
DELAYED PUBERTY
PRIMARY AMENORRHEA
AORTIC DISSECTION
ARTERIAL DISSECTION
EXTERNALEARMALFORMAT.
INVERTED NIPPLES
WEBBED NECK
COARCTATION OF AORTA
HORSESHOE KIDNEY
−2 0 2 4 6
signed log10−scaled p.adjust
core genes
50
100
NES
−2 0 2
B
fXO
mXO1
mXO2
ave.mXO
ave.XO
fmE2
m1m2O
CHOLESTEROLMETABOLISMWITHBLAKP.
CHOLESTEROLBIOSYNTHESISPATHWAY.
MEVALONATEARMOFCHOLESTEROLBIOP.
STEROLREGULATORYELEMENTBINDPSS.
CELL CYCLE
ENDODERM DIFFERENTIATION
HISTONE MODIFICATIONS
DNA DAMAGE RESPONSE
MIRNAREGULATIONOFDNADAMAGERESP.
MALIGNANT PLEURAL MESOTHELIOMA
SREBFANDMIR33INCHOLESTEROLANLH.
PHOTODYNAMICTHERAPYINDUCEDUNPR.
CIRCADIAN RHYTHM GENES
RETINOBLASTOMA GENE IN CANCER
MESODERMAL COMMITMENT PATHWAY
MAPK SIGNALING PATHWAY
OREXIN RECEPTOR PATHWAY
DNAIRDOUBLESTRANDBREAKSANDCRVA.
ENDOCHONDRALOSSIFICATIONWITHSD.
ENDOCHONDRAL OSSIFICATION
FOCALADHESIONPI3KAKTMTORSIGNAP.
CLEARCELLRENALCELLCARCINOMAPAT.
OMEGA9 FATTY ACID SYNTHESIS
ECTODERM DIFFERENTIATION
CCL18 SIGNALING PATHWAY
EXERCISEINDUCEDCIRCADIANREGULA.
TGFBETA SIGNALING PATHWAY
G1 TO S CELL CYCLE CONTROL
RETT SYNDROME CAUSING GENES
DNAIRDAMAGEANDCELLULARRESPONVA.
PRION DISEASE PATHWAY
STATININHIBITIONOFCHOLESTEROLP.
HIPPOMERLINSIGNALINGDYSREGULAT.
HEDGEHOGSIGNALINGPATHWAYWP4249.
TGFBETARECEPTORSIGNALINGINSKED.
INTERACTIONSOFNATURALKILLECIPC.
PHOTODYNAMICTHERAPYINDUCEDAPSS.
MRNA PROCESSING
ARYLHYDROCARBONRECEPTORPATHWAW.
ATM SIGNALING PATHWAY
HEPATITISCANDHEPATOCELLULARCAR.
ANGIOPOIETINLIKEPROTEIN8REGULP.
HEADANDNECKSQUAMOUSCELLCARCINO.
MELATONINMETABOLISMANDEFFECTS.
WNT SIGNALING PATHWAY
EGFRTYROSINEKINASEINHIBITORRES.
NSP1FROMSARSCOV2INHIBITSTIITHC.
TRANSLATION FACTORS
MITOCHONDRIALCOMPLEXIVASSEMBLY.
TYROBPCAUSALNETWORKINMICROGLIA.
MITOCHONDRIALCOMPLEXIASSEMBMOS.
OXIDATIVE PHOSPHORYLATION
ELECTRONTRANSPORTCHAINOXPHOSIM.
CYTOPLASMIC RIBOSOMAL PROTEINS
−10 0 10
signed log10−scaled p.adjust

Figure 3

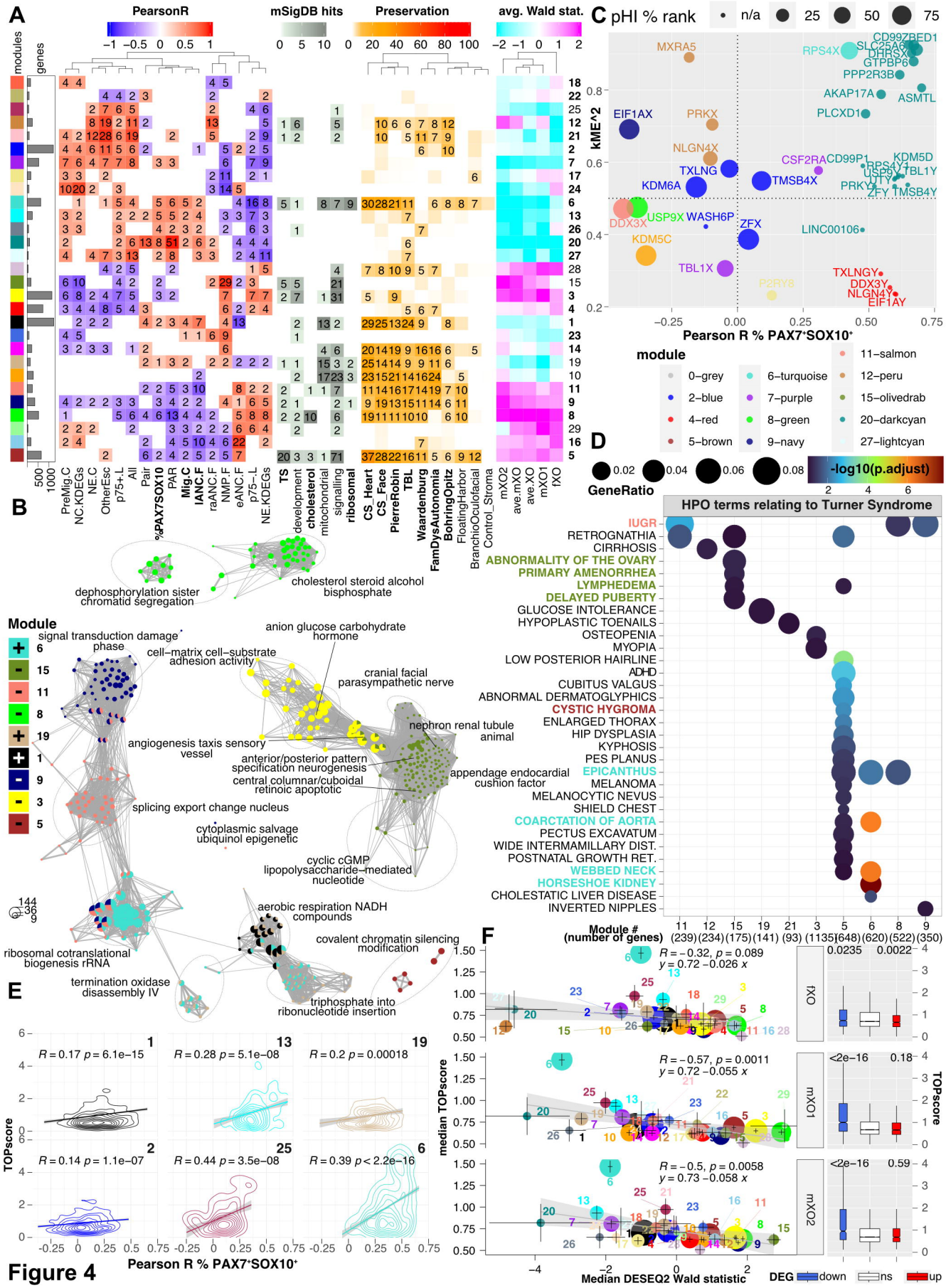
A
PearsonR
mSigDB hits
Preservation
avg. Wald stat.
modules
genes
PreMig.C
NC.KDEGs
NE.C
OtherEsc
p75+.L
All
Pair
%PAX7SOX10
PAR
Mig.C
IANC.F
raANC.F
NMP.F
eANC.F
p75−.L
NE.KDEGs
TS
development
cholesterol
mitochondrial
signalling
ribosomal
CS_Heart
CS_Face
PierreRobin
TBL
Waardenburg
FamDysAutonomia
BohringOpitz
FloatingHarbor
BranchioOculofacial
Control_Stroma
mXO2
ave.mXO
ave.XO
mXO1
fXO
B
dephosphorylation sister chromatid segregation
cholesterol steroid alcohol bisphosphate
C
pHI % rank
n/a
25
50
75
kME^2
Pearson R % PAX7⁺SOX10⁺
MXRA5
RPS4X
CD99
TBED1
SLC25A6
DHRSX
GTPBP6
PPP2R3B
AKAP17A
ASMTL
PLCXD1
EIF1AX
PRKX
NLGN4X
CSF2RA
CD99P1
KDM5D
RPS4Y1
USP9Y
TBL1Y
UTY
PRKY
ZFY
TMSB4Y
TXLNG
TMSB4X
KDM6A
DDX3X
USP9X
WASH6P
ZFX
LINC00106
KDM5C
TBL1X
P2RY8
TXLNGY
DDX3Y
NLGN4Y
EIF1AY
module
0–grey
2–blue
4–red
5–brown
6–turquoise
7–purple
8–green
9–navy
11–salmon
12–peru
15–olivedrab
20–darkcyan
27–lightcyan
D
GeneRatio
-log10(p.adjust)
HPO terms relating to Turner Syndrome
IUGR
RETROGNATHIA
CIRRHOSIS
ABNORMALITY OF THE OVARY
PRIMARY AMENORRHEA
LYMPHEDEMA
DELAYED PUBERTY
GLUCOSE INTOLERANCE
HYPOPLASTIC TOENAILS
OSTEOPENIA
MYOPIA
LOW POSTERIOR HAIRLINE
ADHD
CUBITUS VALGUS
ABNORMAL DERMATOGLYPHICS
CYSTIC HYGROMA
ENLARGED THORAX
HIP DYSPLASIA
KYPHOSIS
PES PLANUS
EPICANTHUS
MELANOMA
MELANOCYTIC NEVUS
SHIELD CHEST
COARCTATION OF AORTA
PECTUS EXCAVATUM
WIDE INTERMAMILLARY DIST.
POSTNATAL GROWTH RET.
WEBBED NECK
HORSESHOE KIDNEY
CHOLESTATIC LIVER DISEASE
INVERTED NIPPLES
Module #
(number of genes)
E
Module
signal transduction damage phase
cell–matrix cell–substrate adhesion activity
anion glucose carbohydrate hormone
cranial facial parasympathetic nerve
nephron renal tubule animal
angiogenesis taxis sensory vessel
anterior/posterior pattern specification neurogenesis
central columnar/cuboidal retinoic apoptotic
appendage endocardial cushion factor
splicing export change nucleus
cytoplasmic salvage ubiquinol epigenetic
cyclic cGMP lipopolysaccharide–mediated nucleotide
aerobic respiration NADH compounds
covalent chromatin silencing modification
ribosomal cotranslational biogenesis rRNA
termination oxidase disassembly IV
triphosphate into ribonucleotide insertion
TOPscore
Pearson R % PAX7⁺SOX10⁺
F
median TOPscore
Median DESEQ2 Wald statistic
DEG
down
ns
up

Figure 4